


1 Weekly to monthly time scale of melt inclusion entrapment
2 prior to eruption  by phosphorus distribution
3 in olivine from mid-ocean ridges

4 **Mélina Manzini^{1*}, Anne-Sophie Bouvier¹, Lukas P. Baumgartner¹, Othmar**
5 **Müntener¹, Estelle F. Rose-Koga², Pierre Schiano², Stéphane Escrig³, Anders**
6 **Meibom^{1,3}, and Nobumichi Shimizu⁴**

7 *¹Institute of Earth Sciences, University of Lausanne, 1015 Lausanne, Switzerland*

8 *²Laboratoire Magmas et Volcans, University of Blaise Pascal–CNRS–IRD, 63038*
9 *Clermont-Ferrand, France*

10 *³Laboratory for Biological Geochemistry, Federal School of Technology Lausanne, 1015*
11 *Lausanne, Switzerland*

12 *⁴Woods Hole Oceanic Institution, Woods Hole, Massachusetts 02543, USA*

13 *E-mail: melina.manzini@unil.ch

14 **ABSTRACT**


15 Melt inclusions (MIs) hosted in euhedral olivine have been proposed to represent
16 droplets of primary melt, protected from processes occurring near Earth's surface during
17 eruption. The complex zoning of phosphorus (P) in some olivines and the presence of a
18 P-depleted zone around MIs indicate a complex history for the host-MI system. We
19 analyzed P in olivine and MIs from two mid-oceanic ridge basalt (MORB) samples from
20 the Mid-Atlantic Ridge (MAR) by electron probe microanalyzer, secondary ion mass
21 spectrometry (SIMS), and NanoSIMS. Phosphorus dendrites in olivine suggest an initial
22 fast olivine growth followed by a stage of slower growth. Dissolution textures around

23 some MIs were identified and were probably caused by adiabatic decompression melting.
24 Based on diffusion modeling of P in olivine, we infer that olivine beneath the MAR
25 remains in the system (1) for days to weeks after crystallization of P-rich lamellae, and
26 (2) for a few hours after recrystallization of dissolved olivine. Dissolution and
27 reprecipitation of olivine containing boundary layers suggests that most MIs might be
28 affected by late post-entrapment processes.

29 INTRODUCTION

30 Olivine-hosted melt inclusions (MIs) are widely used to constrain primary melt
31 compositions because they are isolated from the magma and assumed to preserve the
32 composition of the melt from which their host grew (e.g., Kent, 2008; Métrich and
33 Wallace, 2008; Schiano, 2003). Despite agreement that olivine-hosted MIs are entrapped
34 at relatively shallow levels (<10 km), the origin of melt entrapped in MIs is debated.
35 Some studies indicate that MIs represent the melt composition of the last reequilibration
36 in the mantle (e.g., Hart, 1993; Sobolev, 1996), while others argue that MIs record
37 interaction with the magmatic plumbing system (e.g., Kent et al., 2002; Saal et al., 2005;
38 Kamenetsky and Gurenko, 2007), or localized, grain-scale dissolution-reaction-mixing
39 processes (Danyushevsky et al., 2004). Finally, they can lose their initial water content
40 and change oxygen fugacity (f_{O_2}) (Gaetani and Watson, 2000), calling into question the
41 interpretation that the large compositional variations observed in MIs directly represent
42 the heterogeneity of the mantle source.

43 The idea that euhedral olivine grows in concentric layers from core to rim has
44 been challenged due to the discovery of irregular, rhythmic zonation in incompatible,
45 slow-diffusing elements such as phosphorus (P) (e.g., Milman-Barris et al., 2008; Welsch

46 et al., 2013, 2014). It **has been** suggested that euhedral olivine forms by infilling the
47 spaces of this skeletal **and/or** dendritic framework (Welsch et al., 2013), formed during
48 fast diffusion-controlled growth ($>10^{-6}$ to 10^{-7} cm/s; Jambon et al., 1992), when growth
49 rate slows down (Welsch et al., 2014). It has been demonstrated that MIs formed during
50 diffusion-controlled, rapid skeletal or dendritic growth of olivine may trap surface
51 boundary layers that modify their composition (Faure and Schiano, 2005). It is thus
52 important to understand the timing of MI entrapment. Indeed, P-depleted olivine halos
53 around MIs located close to P-zoned olivine have been described (e.g., Milman-Barris et
54 al., 2008, **Shea et al., 2015**  **[Shea et al., 2015" matches multiple references. Please add**
55 **letters (e.g. "Smith, 2000a").]**, Bouvet de Maisonneuve et al., 2016), suggesting
56 interaction (diffusion or dissolution) between the dendritic olivine and MIs.

57 Phosphorous diffusion is slow compared to **that of** other elements in olivine [log
58 (D_0 , m²/s) = -10.06 ± 0.8 , $E_a = 229 \pm 16$ kJ, **where D_0 is the pre-exponential factor, and**
59 **E_a is activation energy** [Watson et al., 2015], two to four orders of magnitude slower than
60 Fe-Mg interdiffusion in olivine]. Acquisition of P profiles allows the residence time of
61 the olivine in the system to be determined, **as well as** the relative timing of the different
62 processes occurring in the olivine during mineral growth, melt inclusion entrapment, and
63 eruption. Estimated residence times of olivine within the mid-oceanic ridge basalt
64 (MORB) magmatic system based on diffusion modeling of different elements (Ni, Al,
65 Ca, Fe-Mg) has been proposed to be between <1 day and 4 yr, with shorter times being
66 prevalent (e.g., Nabelek and Langmuir, 1986; Zellmer et al., 2011; Colin et al., 2012). P
67 diffusion profiles are therefore expected to be very short, and require **analysis by**
68 **nanoscale secondary ion mass spectrometry (NanoSIMS)**.

69 We combined P X-ray maps and high-spatial-resolution NanoSIMS profiles of P,
70 Al, Mg, and Si with MELTS software (<http://melts.ofm-research.org>) calculations and
71 quantitative measurements of P and major element concentrations in olivine and in their
72 MIs in order to better understand entrapment mechanisms. NanoSIMS profiles of P in
73 olivine allow the residence time of olivine in the system after MI entrapment and before
74 eruption to be estimated. We show that decompression can cause olivine dissolution and
75 MI formation upon reprecipitation on very short time scales.

76 SAMPLES AND ANALYTICAL METHODS

77 The selected olivines contain 50–350 μm glassy MIs and are from two different
78 locations on the Mid-Atlantic Ridge (MAR). The first sample is a dredged olivine-rich
79 picrite (sample ARP73-10-03, 36°8372'N, 33°2482'W) from the FAMOUS zone
80 (Bougault and Hekinian, 1974). This sample contains >20% olivine phenocrysts, rare
81 clinopyroxene, and plagioclase xenocrysts (Laubier et al., 2007). The geological context,
82 geochemistry of lavas, and MIs were described in several studies (e.g., Langmuir et al.,
83 1977; Laubier et al., 2007; Gale et al., 2013). The second sample (CH77-DR6-203) is a
84 dredged fresh basalt containing a high volatile proportion from the 14° MAR triple
85 junction (14.12°N, 45°W) (Bougault et al., 1988; Javoy and Pineau, 1991).

86 Major element composition and X-ray element maps of olivine and MIs (Fig. 1;
87 Fig. DR2 in the GSA Data Repository¹) were acquired by electron probe microanalyzer
88 (EPMA; University of Lausanne, Switzerland). The P content of MIs and olivine was
89 determined by measuring ³¹P and ²⁸Si in monocollection using the CAMECA IMS 1280-
90 HR at the SwissSIMS laboratory (University of Lausanne). High-resolution ³¹P, ²⁸Si, Al
91 (²⁷Al¹⁶O), and Mg (²⁴Mg¹⁶O) profiles were acquired with a CAMECA NanoSIMS 50L

92 (École Polytechnique Fédérale de Lausanne, Switzerland) (Fig. 1; Fig. DR3). ^{31}P
93 measurements were normalized to ^{28}Si , measured at the same time, in order to monitor
94 possible instrumental drift. Analytical solutions to the one-dimensional diffusion equation
95 were used to obtain least-square fits to the normalized profiles and determine the
96 residence time of olivine in the system both (1) after the crystallization of P-rich lamellae
97 and (2) after the dissolution event (Fig. 2). Uncertainties reported for calculated diffusion
98 time scales are from the fitting procedure and do not include the uncertainty of the
99 diffusion coefficient for P in olivine (Watson et al., 2015). Analytical details for all
100 methods are provided in the Data Repository.

101 RESULTS

102 Within each MI, the major element composition is homogeneous, except for a
103 slight Mg and Fe depletion along the 5–8- μm -wide MI wall (Fig. DR2). The studied parts
104 of olivine crystals do not show any significant chemical zoning except for P, which
105 outlines a dendritic pattern (Fig. 1; Fig. DR2). Nine of the 15 mapped olivine crystals
106 from both samples show P zoning. MIs were trapped in both P-zoned (containing P-rich
107 olivine lamellae) and unzoned areas of olivine. All MIs located in P-zoned domains have
108 a P-depleted halo, which has a variable and irregular shape truncating the P-rich lamellae.
109 Based on two-dimensional estimates on X-ray maps, the volume of the surrounding P-
110 depleted halo is at least as **much** as **that** of the MI. P concentrations in olivine are 30–
111 1200 ppm, and in MI, 300–500 ppm (Fig. 1).

112 At the olivine-MI boundary, the difference in composition between melt and
113 olivine on NanoSIMS profiles is reflected by a gradual decrease in $^{24}\text{Mg}/^{28}\text{Si}$ and increase
114 in $^{27}\text{Al}/^{28}\text{Si}$ and $^{31}\text{P}/^{28}\text{Si}$ ratios (Fig. DR3), likely due to the geometry of the inclusion

115 walls. The $^{31}\text{P}/^{28}\text{Si}$ transition (Fig. 1; Fig. DR3) is too wide to be the result of this
116 geometry only and is likely related to growth kinetics, primarily affecting P, as it diffuses
117 more slowly than Mg or Al in the melt (Spandler et al., 2007; Chakraborty, 2010; Watson
118 et al., 2015). The small P-enriched zone (Fig. 1, profile 4) around the MI corresponds to
119 post-entrapment growth of olivine. The gradational variation in P concentration between
120 lamellae in the P-zoned olivine most likely represents diffusion profiles, whereas the
121 transition between P-depleted halo and P-zoned or unzoned olivine domains is sharp (Fig.
122 1; Fig. DR3).


123 **DISCUSSION**

124 A key observation is the systematic finding of a P-depleted halo around MIs
125 hosted in direct contact with P-rich olivine. This halo truncates the P-rich zoning (e.g.,
126 Fig. 1; Fig. DR2). Different processes could form P-depleted halos (Milman-Barris et al.,
127 2008): (1) slow olivine crystallization on the wall of a melt pool; (2) dissolution and
128 reprecipitation of olivine; or (3) diffusion of P between olivine and MI. The sharp
129 truncations of the P-zoned domains (Fig. 1) by the halo do not support the first and third
130 hypotheses. Also, the preservation of P-rich lamellae on the micrometer scale does not
131 support the formation of diffusion halos over tens of micrometers, because the bands
132 should also broaden at the same rate. Based on the irregular shape of the P-depleted halo
133 and the clear truncation of the P zonation (Fig. 1), a coupled dissolution and
134 reprecipitation mechanism is more likely (e.g., Milman-Barris et al., 2008). Dissolution
135 of olivine is favored along fractures **and** defect zones, **and** around high-energy surfaces
136 **like** MIs and embayments. Dissolution can be triggered by increase in temperature,
137 mixing of melts with different composition, decompression, increase of volatile content

138 in the melt, or a combination of these processes. H₂O input may induce dissolution by
139 lowering the melting temperature. In MORB settings, H₂O input is limited, and the
140 similar composition of MIs and olivine domains suggests neither fluid input nor mixing
141 of significantly different melts. As olivine is compositionally homogeneous (Fig. DR2)
142 and the different MIs hosted in a single olivine grain have similar composition (Table
143 DR2 in the Data Repository), temperature increase is an unlikely cause for olivine
144 dissolution. MI migration by dissolution of the olivine in front of the MI and
145 reprecipitation of olivine behind the MI requires temperature gradients in the mineral
146 (Schiano et al., 2006). Such a migration process could also create P-depleted halos
147 around MIs. Even if the presence of P-depleted halos around melt embayments has been
148 observed in olivine crystallization experiments by cooling of a single melt at constant
149 pressure (Milman-Barris et al., 2008), we do not favor dissolution triggered by increase in
150 temperature, as it seems unlikely that the necessary temperature gradient is present on the
151 crystal scale. We would expect to see temperature-induced zoning, inconsistent with the
152 homogeneity of the studied olivines. The third possibility for dissolution of olivine is
153 adiabatic decompression. Simple MELTS calculations (Ghiorso and Sack, 1995; Ghiorso
154 et al., 2002) demonstrate that moderate decompression (<2 kbar) can dissolve ~15%–
155 30% of the olivine (Table DR3; Fig. DR4), while affecting the forsterite content by
156 <0.7%. As the P-depleted halos represent only a small volume of the total olivine, the
157 required decompression is <2 kbar.

158 The MIs shown in Figure 1 were all entrapped during a slow crystal growth
159 period, as they have similar compositions. Indeed, if MIs “a” and “b” (Fig. 1) were
160 trapped during a period of fast growth, they would be enriched in elements incompatible

161 in olivine such as CaO or Al₂O₃ (Faure and Schiano, 2005). They can be trapped either
162 during initial olivine growth (called case 1 hereafter) or during dissolution-precipitation
163 along defects (case 2). For case 1, it is unlikely that pressure changes would be
164 transferred into the fully enclosed MI. Even if it was the case, local disequilibrium
165 between MI and the P-rich olivine would facilitate dissolution of the P-rich lamellae only
166 during decompression, a feature not observed here. In case 2, an olivine melt pocket is
167 connected with the surrounding melt in an open system (embayment). Decompression
168 induces dissolution of P-zoned and unzoned olivine. The dissolution of P-zoned olivine
169 will locally enrich the melt in P. As P diffusion in melt is slow and P is incompatible, the
170 new melt will locally have a higher P content. Subsequent temperature drop causes
171 olivine crystallization and entrapment of the MI. Our data favor the open-system
172 hypothesis.

173 NanoSIMS profiles across the P-rich dendrites highlight P diffusion in olivine.
174 Based on these diffusion profiles and on the diffusion coefficient from Watson et al.
175 (2015), we estimate that at 1270 °C, olivine can remain in the system for about ~1 week
176 (7.5 ± 0.3 days, based on profile 9 [P9] from ARP73-10-03_16; Fig. 2) prior to eruption,
177 in agreement with previously estimated short residence times for MORB samples (e.g.,
178 Nabelek and Langmuir, 1986; Danyushevsky et al., 2002; Pan and Batiza, 2002; Zellmer
179 et al., 2011; Colin et al., 2012). A temperature of 1270 °C was chosen based on results
180 from sample ARP73-10-03[[Cor

Page 8 of 18

184 residence time of olivine remains short (~2 weeks at 1200 °C and ~2 months at 1100 °C).
185 The sharp boundary between P-zoned olivine and the P-depleted halo located around MIs
186 (profiles 4 and 7; Fig. 1) suggests olivine residence times of a few hours during MI
187 inclusion.

188 In summary, our data suggest that growth of some olivine crystals is initially
189 diffusion controlled, as reflected by P zoning (Fig. 3, stage 1), followed by interface-
190 controlled growth (Fig. 3, stage 2) (Welsch et al., 2014). During its ascent to the surface,
191 olivine starts dissolving, preferentially around embayment or along fracture/defect zones
192 (Fig. 3, stage 3), probably due to adiabatic decompression. Decreasing temperature
193 and/or degassing of the melt during ascent increases the temperature difference from the
194 liquidus (Applegarth et al., 2013), leading to reprecipitation of a P-depleted olivine and
195 the preservation of MIs with elevated P contents (Fig. 3, stage 4) at an interface-
196 controlled slow growth rate in the last hours before the olivine reaches the surface.
197 Olivine crystallizing at the wall of the MI, seen in almost all MIs (e.g., Kent, 2008), is
198 highly enriched in P, as shown in the NanoSIMS profiles, suggesting fast growth for this
199 last process (Fig. 3, stage 5).

200 CONCLUSIONS



201 Olivine dissolution-precipitation during **[[Missing part of sentence here**
202 **(including verb)]]**, as a P-poor halo around MIs has been observed in olivine from two
203 MORB samples studied here, as well as in olivine from different settings (e.g., Milman-
204 Barris et al., 2008; Welsch et al., 2014). Phosphorous concentration maps of olivine
205 combined with NanoSIMS P profiles strongly suggest that olivine, after skeletal growth,
206 remains for a few days in the system, and that MIs are enclosed only shortly (hours)

207 before eruption. MI composition can be affected by olivine dissolution and
208 recrystallization processes, at least for P, and cannot be simply taken as representative of
209 the mantle source. Care should thus be taken when interpreting MI P and other
210 incompatible element compositional variability.

211 **ACKNOWLEDGMENTS**

212 We acknowledge funding by the KIP6 PCI to Baumgartner and Manzini, and
213 constructive comments from J. Hammer, B. Welsch, and A. Kent. Rose-Koga
214 acknowledges financial support from the Centre National de la Recherche Scientifique
215 (SYSTER).

216 **REFERENCES CITED**



- 217 Applegarth, L.J., Tuffen, H., James, M.R., and Pinkerton, H., 2013, Degassing-driven
218 crystallisation in basalts: *Earth-Science Reviews*, v. 116, p. 1–16,
219 <https://doi.org/10.1016/j.earscirev.2012.10.007>.
- 220 Bougault, H., and Hekinian, R., 1974, Rift valley in the Atlantic Ocean near 36°50'N:
221 Petrology and geochemistry of basaltic rocks: *Earth and Planetary Science Letters*,
222 v. 24, p. 249–261, [https://doi.org/10.1016/0012-821X\(74\)90103-4](https://doi.org/10.1016/0012-821X(74)90103-4).
- 223 Bougault, H., Dmitriev, L., Schilling, J.G., Sobolev, A., Joron, J.L., and Needham, H.D.,
224 1988, Mantle heterogeneity from trace elements: MAR triple junction near 14°N:
225 *Earth and Planetary Science Letters*, v. 88, p. 27–36, [https://doi.org/10.1016/0012-821X\(88\)90043-X](https://doi.org/10.1016/0012-821X(88)90043-X).
- 227 Bouvet de Maisonneuve, C., Costa, F., Huber, C., Vonlanthen, P., Bachmann, O., and
228 Dungan, M.A., 2016, How do olivines record magmatic events? Insights from major

- 229 and trace element zoning: *Contributions to Mineralogy and Petrology*, v. 171, 56,
230 <https://doi.org/10.1007/s00410-016-1264-6>.
- 231 Chakraborty, S., 2010, Diffusion coefficients in olivine, wadsleyite and ringwoodite:
232 *Reviews in Mineralogy and Geochemistry*, v. 72, p. 603–639,
233 <https://doi.org/10.2138/rmg.2010.72.13>.
- 234 Colin, A., Faure, F., and Burnard, P., 2012, Timescales of convection in magma
235 chambers below the Mid-Atlantic ridge from melt inclusions investigations:
236 *Contributions to Mineralogy and Petrology*, v. 164, p. 677–691,
237 <https://doi.org/10.1007/s00410-012-0764-2>.
- 238 Danyushevsky, L.V., Della, F.N., and Sokolov, S., 2000, Re-equilibration of melt
239 inclusions trapped by magnesian olivine phenocrysts from subduction-related
240 magmas: Petrological implications: *Contributions to Mineralogy and Petrology*,
241 v. 138, p. 68–83, <https://doi.org/10.1007/PL00007664>.
- 242 Danyushevsky, L.V., Sokolov, S., and Falloon, T.J., 2002, Melt inclusions in olivine
243 phenocrysts: Using diffusive re-equilibration to determine the cooling history of a
244 crystal, with implications for the origin of olivine-phyric volcanic rocks: *Journal of*
245 *Petrology*, v. 43, p. 1651–1671, <https://doi.org/10.1093/petrology/43.9.1651>.
- 246 Danyushevsky, L.V., Leslie, R.A.J., Crawford, A.J., and Durance, P., 2004, Melt
247 inclusions in primitive olivine phenocrysts: The role of localized reaction processes
248 in the origin of anomalous compositions: *Journal of Petrology*, v. 45, p. 2531–2553,
249 <https://doi.org/10.1093/petrology/egh080>.

- 250 Faure, F., and Schiano, P., 2005, Experimental investigation of equilibration conditions
251 during forsterite growth and melt inclusion formation: *Earth and Planetary Science*
252 *Letters*, v. 236, p. 882–898, <https://doi.org/10.1016/j.epsl.2005.04.050>.
- 253 Gaetani, G.A., and Watson, E.B., 2000, Open system behavior of olivine-hosted melt
254 inclusions: *Earth and Planetary Science Letters*, v. 183, p. 27–41,
255 [https://doi.org/10.1016/S0012-821X\(00\)00260-0](https://doi.org/10.1016/S0012-821X(00)00260-0).
- 256 Gale, A., Laubier, M., Escrig, S., and Langmuir, C.H., 2013, Constraints on melting
257 processes and plume-ridge interaction from comprehensive study of the FAMOUS
258 and North Famous segments, Mid-Atlantic Ridge: *Earth and Planetary Science*
259 *Letters*, v. 365, p. 209–220, <https://doi.org/10.1016/j.epsl.2013.01.022>.
- 260 Ghiorso, M.S., and Sack, R.O., 1995, Chemical mass transfer in magmatic processes IV:
261 A revised and internally consistent thermodynamic model for the interpolation and
262 extrapolation of liquid-solid equilibria in magmatic systems at elevated temperatures
263 and pressures: *Contributions to Mineralogy and Petrology*, v. 119, p. 197–212,
264 <https://doi.org/10.1007/BF00307281>.
- 265 Ghiorso, M.S., Hirschmann, M.M., and Reiners, P.W., 2002, The pMELTS: A revision of
266 MELTS for improved calculation of phase relations and major element partitioning
267 related to partial melting of the mantle to 3 GPa: *Geochemistry Geophysics*
268 *Geosystems*, v. 3, p. 1–35, <https://doi.org/10.1029/2001GC000217>.
- 269 Hart, S.R., 1993, Equilibration during mantle melting: A fractal tree model: *Proceedings*
270 *of the National Academy of Sciences of the United States of America*, v. 90,
271 p. 11,914–11,918.

- 272 Jambon, A., Lussiez, P., Clocchiatti, R., Weisz, J., and Hernandez, J., 1992, Olivine
273 growth rates in a tholeiitic basalt: An experimental study of melt inclusions in
274 plagioclase: *Chemical Geology*, v. 96, p. 277–287, [https://doi.org/10.1016/0009-](https://doi.org/10.1016/0009-2541(92)90059-E)
275 2541(92)90059-E.
- 276 Javoy, M., and Pineau, F., 1991, The volatiles record of a “popping” rock from the Mid-
277 Atlantic Ridge at 14°N: Chemical and isotopic composition of gas trapped in the
278 vesicles: *Earth and Planetary Science Letters*, v. 107, p. 598–611,
279 [https://doi.org/10.1016/0012-821X\(91\)90104-P](https://doi.org/10.1016/0012-821X(91)90104-P).
- 280 Kamenetsky, V.S., and Gurenko, A.A., 2007, Cryptic crustal contamination of MORB
281 primitive melts recorded in olivine-hosted glass and mineral inclusions:
282 *Contributions to Mineralogy and Petrology*, v. 153, p. 465–481,
283 <https://doi.org/10.1007/s00410-006-0160-x>.
- 284 Kent, A.J.R., 2008, Melt inclusions in basaltic and related volcanic rocks: Reviews in
285 *Mineralogy and Geochemistry*, v. 69, p. 273–331,
286 <https://doi.org/10.2138/rmg.2008.69.8>.
- 287 Kent, A.J.R., Baker, J.A., and Wiedenbeck, M., 2002, Contamination and melt
288 aggregation processes in continental flood basalts: Constraints from melt inclusions
289 in Oligocene basalts from Yemen: *Earth and Planetary Science Letters*, v. 202,
290 p. 577–594, [https://doi.org/10.1016/S0012-821X\(02\)00823-3](https://doi.org/10.1016/S0012-821X(02)00823-3).
- 291 Langmuir, C.H., Bender, J.F., Bence, A.E., Hanson, G.N., and Taylor, S.R., 1977,
292 Petrogenesis of basalts from the FAMOUS area: Mid-Atlantic Ridge: *Earth and*
293 *Planetary Science Letters*, v. 36, p. 133–156, [https://doi.org/10.1016/0012-](https://doi.org/10.1016/0012-821X(77)90194-7)
294 821X(77)90194-7.

- 295 Laubier, M., Schiano, P., Doucelance, R., Ottolini, L., and Laporte, D., 2007, Olivine-
296 hosted melt inclusions and melting processes beneath the FAMOUS zone (Mid-
297 Atlantic Ridge): *Chemical Geology*, v. 240, p. 129–150,
298 <https://doi.org/10.1016/j.chemgeo.2007.02.002>.
- 299 Métrich, N., and Wallace, P.J., 2008, Volatile abundances in basaltic magmas and their
300 degassing paths tracked by melt inclusions: *Reviews in Mineralogy and*
301 *Geochemistry*, v. 69, p. 363–402, <https://doi.org/10.2138/rmg.2008.69.10>.
- 302 Milman-Barris, M.S., Beckett, J.R., Baker, M.B., Hofmann, A.E., Morgan, Z., Crowley,
303 M.R., Vielzeuf, D., and Stolper, E., 2008, Zoning of phosphorus in igneous olivine:
304 *Contributions to Mineralogy and Petrology*, v. 155, p. 739–765,
305 <https://doi.org/10.1007/s00410-007-0268-7>.
- 306 Nabelek, P.I., and Langmuir, C.H., 1986, The significance of unusual zoning in olivines
307 from FAMOUS area basalt 527-1-1: *Contributions to Mineralogy and Petrology*,
308 v. 93, p. 1–8, <https://doi.org/10.1007/BF00963580>.
- 309 Pan, Y., and Batiza, R., 2002, Mid-ocean ridge magma chamber processes: Constraints
310 from olivine zonation in lavas from the East Pacific Rise at 9°30'N and 10°30'N:
311 *Journal of Geophysical Research. Solid Earth*, v. 107,
312 <https://doi.org/10.1029/2001JB000435>.
- 313 Saal, A.E., Hart, S.R., Shimizu, N., Hauri, E.H., Layne, G.D., and Eiler, J.M., 2005, Pb
314 isotopic variability in melt inclusions from the EMI-EMII-HIMU mantle end-
315 members and the role of the oceanic lithosphere: *Earth and Planetary Science*
316 *Letters*, v. 240, p. 605–620, <https://doi.org/10.1016/j.epsl.2005.10.002>.

- 317 Schiano, P., 2003, Primitive mantle magmas recorded as silicate melt inclusions in
318 igneous minerals: *Earth-Science Reviews*, v. 63, p. 121–144,
319 [https://doi.org/10.1016/S0012-8252\(03\)00034-5](https://doi.org/10.1016/S0012-8252(03)00034-5).
- 320 Schiano, P., Provost, A., Clocchiatti, R., and Faure, F., 2006, Transcrystalline melt
321 migration and Earth's mantle: *Science*, v. 314, p. 970–974,
322 <https://doi.org/10.1126/science.1132485>.
- 323 **[[There are two references that could be cited as Shea, et al, 2015. Please use a,b**
324 **extensions to dates of the following two references.]]**
- 325 **Shea**, T., Costa, F., Krimer, D., and Hammer, J.E., , Accuracy of timescales
326 retrieved from diffusion modeling in olivine: A 3D perspective: *The American*
327 *Mineralogist*, v. 100, p. 2026–2042, <https://doi.org/10.2138/am-2015-5163>.
- 328 **Shea**, T., Lynn, K.J., and Garcia, M.O., , Cracking the olivine zoning code:
329 Distinguishing between crystal growth and diffusion: *Geology*, v. 43, p. 935–938,
330 <https://doi.org/10.1130/G37082.1>.
- 331 Sobolev, A.V., 1996, Melt inclusions in minerals as a source of principle petrological
332 information: *Petrology*, v. 4, p. 228–239.
- 333 Spandler, C., O'Neill, S.H.C., and Kamenetsky, V.S., 2007, Survival times of anomalous
334 melt inclusions from element diffusion in olivine and chromite: *Nature*, v. 447,
335 p. 303–306, <https://doi.org/10.1038/nature05759>.
- 336 Watson, E.B., Cherniak, D.J., and Holycross, M.E., 2015, Diffusion of phosphorus in
337 olivine and molten basalt: *The American Mineralogist*, v. 100, p. 2053–2065,
338 <https://doi.org/10.2138/am-2015-5416>.

- 339 Welsch, B., Faure, F., Famin, V., Baronnet, A., and Bachèlery, P., 2013, Dendritic
340 crystallization: A single process for all the textures of olivine in basalts?: Journal of
341 Petrology, v. 54, p. 539–574, <https://doi.org/10.1093/petrology/egs077>.
- 342 Welsch, B., Hammer, J., and Hellebrand, E., 2014, Phosphorus zoning reveals dendritic
343 architecture of olivine: Geology, v. 42, p. 867–870,
344 <https://doi.org/10.1130/G35691.1>.
- 345 Zellmer, G.F., Rubin, K.H., Dulski, P., Iizuka, Y., Goldstein, S.L., and Perfit, M.R.,
346 2011, Crystal growth during dike injection of MOR basaltic melts: Evidence from
347 preservation of local Sr disequilibria in plagioclase: Contributions to Mineralogy and
348 Petrology, v. 161, p. 153–173, <https://doi.org/10.1007/s00410-010-0518-y>.


349 **FIGURE CAPTIONS**

350 Figure 1. Electron probe microanalyzer (EPMA) phosphorus (P) elemental X-ray map of
351 olivine ARP73-10-03_16. P concentrations were determined quantitatively by secondary
352 ion mass spectrometry (SIMS). Note higher P concentration in melt inclusions (MIs)
353 situated near P-zoned olivine compared to ones located in P-unzoned olivine. Pink arrows
354 represent nanoscale SIMS (NanoSIMS) profiles; arrow indicates direction of profile, and
355 number is profile number. NanoSIMS profiles used ~150-nm-diameter beam. $^{31}\text{P}/^{28}\text{Si}$
356 profiles 4, 7, and 9 are located at boundary between MI and olivine (profiles 4 and 7) and
357 in olivine (profile 9). Interface between MI and olivine was determined based on Al and
358 Mg NanoSIMS profiles (Fig. DR3 [see footnote 1]). Peak in rectangle in profile 9 is peak
359 fitted in Figure 2. Peak situated at 47 μm in profile 9 is originally composed of three
360 lamellae (indicated by gray rectangles). Because their diffusion profiles overlap, they
361 were not fitted.

362

363 Figure 2. Comparison of measured $^{31}\text{P}/^{28}\text{Si}$ profile in olivine ARP73-10-03_16 (see Fig. 1
364 for profile location) with calculated curve derived from point-source diffusion modeling.
365 Note excellent fit. Diffusion was ~8 days at $1270\text{ }^{\circ}\text{C}$ [Define “ $t_{1270^{\circ}\text{C}}$ ”], using diffusion
366 coefficient from Watson et al. (2015). This is a maximum estimate for temperature,
367 because an infinitesimally small point source was assumed.

368

369 Figure 3. Schematic evolution of olivine crystal and melt inclusion (MI) entrapment in
370 (100) section. Phosphorus content during different steps of olivine growth and MI
371 entrapment is shown schematically on the profiles. Stages 1 and 2 correspond to growth
372 of dendritic olivine followed by overgrowth of dendrites, leading to formation of
373 euhedral olivine. Melt may be entrapped at this growth stage. Stage 3 illustrates partial
374 olivine dissolution due to adiabatic decompression melting. P-zoned olivine domain
375 might be dissolved at this stage. P-depleted halo will then recrystallize at slow growth
376 rate (stage 4), passively enriching MIs in P. Once olivine rapidly cools (stage 5),
377 remaining melt will be quenched and will form glassy MI. Submicron layer of olivine
378 might crystallize at MI wall and will be enriched in P.  the figure, correct the
379 spelling of “crystallization”; check the location of the right-hand arrow in the “stage
380 3” panel – should it point to the orange area?]]

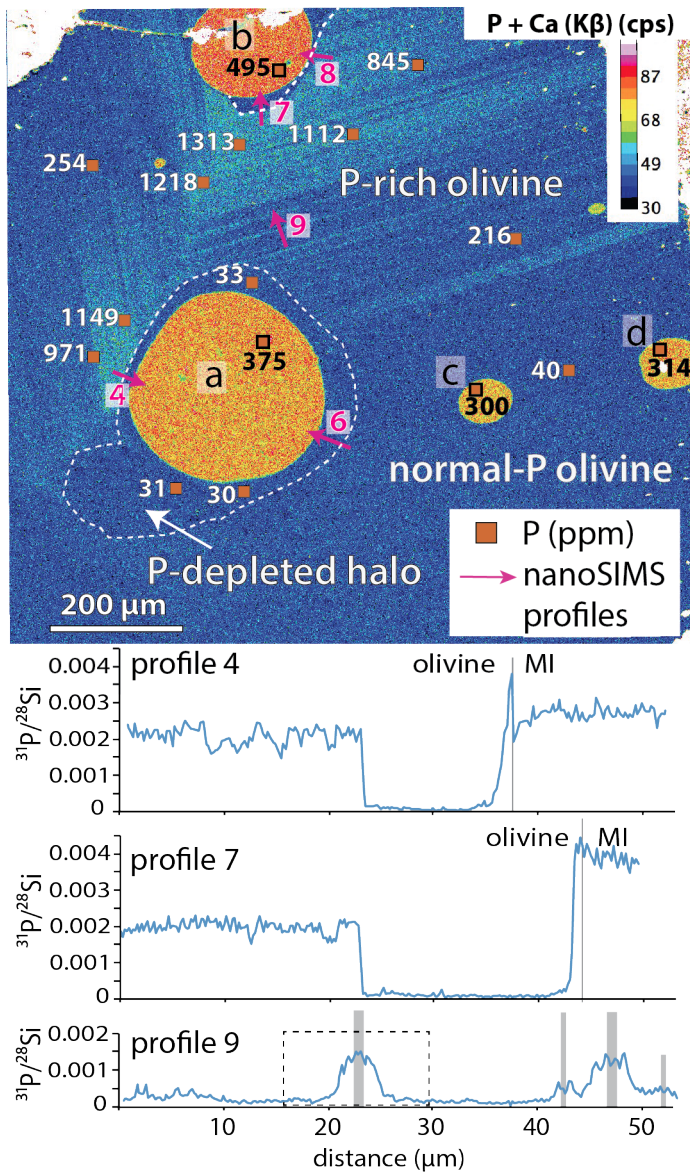
381

382 ¹GSA Data Repository item 2017xxx, additional information about the sample
383 preparation and EPMA, SIMS, and NanoSIMS measurements, as well as information
384 about fitting parameters, is available online at

Publisher: GSA
Journal: GEOL: Geology
DOI:10.1130/G39463.1

385 <http://www.geosociety.org/datarepository/2017/> or on request from
386 editing@geosociety.org.

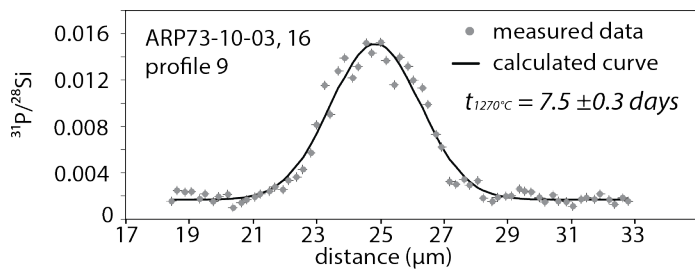
1 **FIGURE CAPTIONS**



2

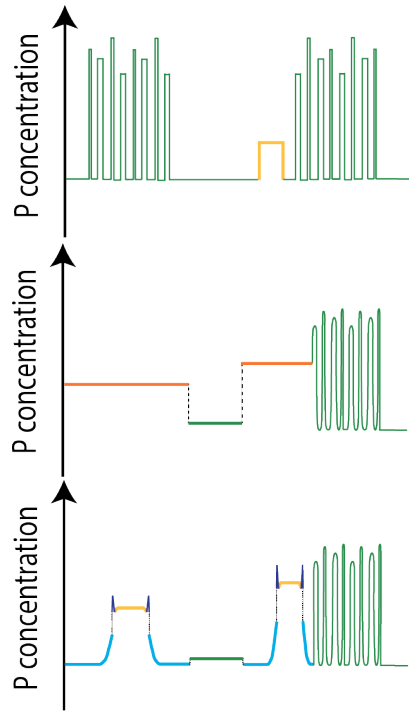
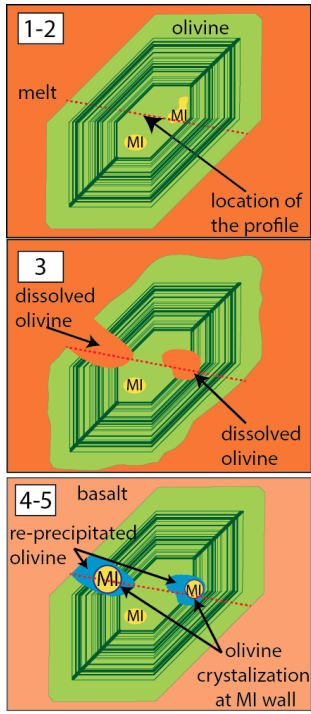
3 Figure 1

4



5

6 Fig.2



7

8 Fig.3

9

1 **Supplementary data**

2

3 **Methodology**

4 *Sample preparation*

5 Polished olivine grains with melt inclusions exposed at the surface were pressed into 1-inch
6 indium mounts. Different glasses and San Carlos olivine were added to the sample mount to
7 be used as reference material for P content determination by SIMS (see below).

8 To ensure that the melt inclusions were totally glassy, we acquired SEM images with a Tescan
9 Mira LMU scanning electron microscope at the University of Lausanne.

10

11 *Electron microprobe*

12 All samples were analyzed by a JEOL 8200 Superprobe at the University of Lausanne.
13 Analytical conditions for major element measurements in olivine were 15kV acceleration
14 voltage, 20nA beam current and 5 μm beam size. Counting time was 30 sec for Si, Mg, Mn,
15 Al and Fe and 40 sec for Ca, Ni and Cr. Natural minerals and synthetic oxides were used as
16 standards. Analytical conditions for major element analyses in melt inclusions were 15kV,
17 10nA and 10 μm . Counting time was 30 sec on all elements, except for K (20 sec) and Na (16
18 sec). A glass standard (KL2-G) was used for SiO_2 , Al_2O_3 . Other elements were calibrated on
19 specific minerals (e.g., a fayalite for Fe). ML3B-G was used as internal standard to check the
20 calibration. Post-entrapment modification due to olivine crystallization (PEC% (% olivine

21 added), Table DR1) at the wall of melt inclusion was corrected for using the Petrolog software
22 (Danyushevsky et al., 2000, 2002; Danyushevsky and Plechov, 2011).

23 X-rays distribution maps of melt inclusions and olivines were acquired by electron
24 microprobe using a JEOL 8200 Superprobe at University of Lausanne. Analytical conditions
25 were 15 kV, 10 nA, 0-1 μm probe diameter and 100 ms dwell-time with a 1-2 μm pixel size
26 for major elements and 15kV, 200-250nA, 0-1 μm probe diameter and 100-230 ms dwell-time
27 with a 1 μm pixel size for P, Al, Ni and Ca. X-ray elemental maps display higher count rate
28 for P in MI compared to P-zoned olivine, as a result of the overlapping of the Ca ($K\beta$) second
29 order peak with the P ($K\alpha$) peak. As olivine contains much less Ca than glass, the interference
30 is negligible in olivine but not in MI. In any case, as olivine is homogeneous in Ca (Figure
31 DR2), the structure on the phosphorus maps and profiles are only caused by variable P
32 concentrations.

33

34

35 **Secondary ion mass spectrometer**

36 P concentrations in olivines and melt inclusions were analysed using a Cameca 1280-HR
37 SIMS at the SwissSIMS laboratory (Lausanne, Switzerland). San Carlos (P = 40 ppm; Welsch
38 et al., 2014) was used as standard for the olivine and BHVO-2G, BCR-2G, BIR-1G (P
39 concentrations are from the certified values furnished by USGS) for the melt inclusions.
40 Samples were sputtered with a 10 kV $^{133}\text{Cs}^+$ primary beam of 1 nA. Electron gun was used to
41 compensate sample charge. A 15 μm raster was used during pre-sputtering (90 sec) and
42 analyses. Counting time was 0.48 s on 29.9 (background), 1.04 s on ^{30}Si and 2.96 sec on ^{31}P .
43 Waiting time was 0.8 s between each mass. Total time for each analysis was <6 min,
44 including automatic centering of the secondary beam. ^{30}Si and ^{31}P were detected on an axial
45 electron multiplier. Entrance slit was set to 60 μm and exit slit to 200 μm , resulting in ~6000
46 mass resolving power. Field aperture was closed to 4000 μm . Energy slit was 50 eV.

47 Uncertainty on each point measurement (internal error) was < 5% (2σ %, average uncertainty
48 of 0.95% 2σ) for P in olivine and <0.8% (2σ %, average uncertainty of 0.2% 2σ) in melt
49 inclusion. The difference in reproducibility is due to counting statistic, melt inclusions having
50 100 times more counts on P. Reproducibility on the standard was < 4.5% (2SD) on the San
51 Carlos and <1% (2SD) on BCR-2G.

52

53 **Nanoscale secondary ion mass spectrometer**

54 Profiles in olivines were obtained using the NanoSIMS at the Center of Advanced Surface
55 Analysis (CASA, Lausanne, Switzerland). A Cs^+ primary beam was used to sputter olivine
56 and the ion species $^{16}\text{O}^-$, $^{28}\text{Si}^-$, $^{31}\text{P}^-$, $^{24}\text{Mg}^{16}\text{O}^-$, $^{27}\text{Al}^{16}\text{O}^-$ and $^{31}\text{P}^{16}\text{O}^-$ were extracted and measured
57 using electron multipliers. In order to prevent the build-up of a charge on the sample's
58 surface, the surfaces were coated with a 10-15nm gold layer. MRP was > 8000 and no peak
59 overlap was observed.

60 After identification of the area of interest using the CCD camera of the NanoSIMS, a 25 x 25
61 μm image of the area of interest was first acquired (with a 256 x 256 pixel resolution
62 corresponding to a pixel size ~ 100 nm). Using the NanoSIMS software, the locations of the
63 linescan were precisely selected to be perpendicular to the transition identified by EMPA
64 analyses. The line scans were acquired using a two-step approach. First a pre-sputtering phase
65 was performed for 2 cycles with a dwell time of 2sec/pixel, using slightly larger beam size to
66 clean up the surface (diaphragm D1-2, and 3.8pA for the Cs^+ primary beam). The acquisition
67 of the high resolution line scans were performed using a finer beam (D1-3, $\sim 150\text{nm}$, and
68 1.7pA for the Cs^+ beam) over 5 cycles with 2sec/pixel. $^{24}\text{Mg}^{16}\text{O}^-$ data were used to monitor
69 possible local variation in the ionization and extraction processes as it is expected to be
70 homogeneous in the olivine measured. ^{16}O , ^{18}O , ^{24}Mg , ^{27}Al , ^{28}Si , ^{31}P and $^{31}\text{P}^{16}\text{O}$ were
71 acquired at the same time. In order to minimize the instrumental drift, we normalized the
72 profiles to ^{28}Si , which is, based on EMPA X-ray maps, homogeneous within the olivine and

73 the MI. The NanoSIMS session was not standardized, resulting in a ^{31}P count rate higher in
74 the MI than in P-zoned olivine, due to matrix effects.

75

76 **Diffusion Chronometry and Fit of Diffusion Profiles**

77 The 2D profiles were measured perpendicular to the zonation. The following parameters were
78 assumed for the diffusion calculations and fitting of the profiles: 1- each P-enriched band was
79 homogeneous at the beginning or represents a line source; 2- the contact between the P-rich
80 and P-poor zones was a step function. Thin, linear features with no plateau were modelled as a
81 line source, while P-enriched zones displaying a plateau were modeled as step functions.
82 Specifically, a P-peak of a few μm width (e.g. Fig. 2) was modelled as line source, while b) P-
83 enriched zones larger than $10\ \mu\text{m}$ were modelled as individual step functions (e.g. Fig. DR5).

84 We used the diffusion coefficient for P diffusion in olivine reported by Watson et al. (2015)
85 based on their diffusion experiments in olivine which are $\log(D_0, \text{m}^2/\text{s}) = -10.06 \pm 0.80$ and E_a
86 $= 229 \pm 16$ kJ/mol. Error functions were fit to each of the measured profiles using a weighted
87 Marquardt fitting routine (Press et al., 1992).

88 The uncertainty of the fit was estimated using the χ^2 per point. The uncertainty, expressed as
89 2σ , for each point was estimated from the variation in the part of the profiles considered to be
90 flat. Initial conditions of the model are the bigger source of uncertainty. Since the line source
91 diffusion modeling assumes an infinite band width of P-enrichment, the calculated values are
92 maximum time estimates.

93

94 **MELTS calculations**

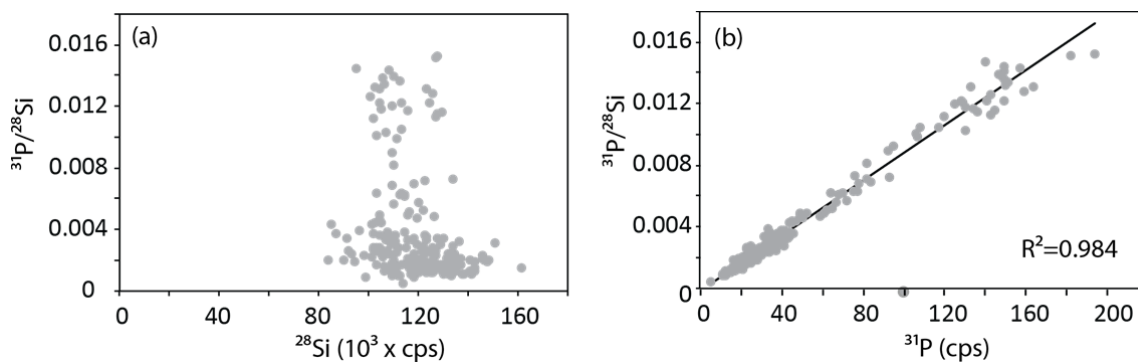
95 MELTs version 5.0 was used. The principles of the program are summarised in Ghiorso and
96 Sack (1995). We used the average composition of the individual melt inclusions and 0.15 wt%
97 H_2O . We then determined the liquidus temperature, followed by decompression calculations
98 slightly below the liquidus temperature. Isentropic, isenthalpic and isothermal decompression

99 calculations were done between 2 kbar and 0.1 kbar in steps of 0.1 kbar, with a fixed fO_2
100 (QFM -2).

101
102

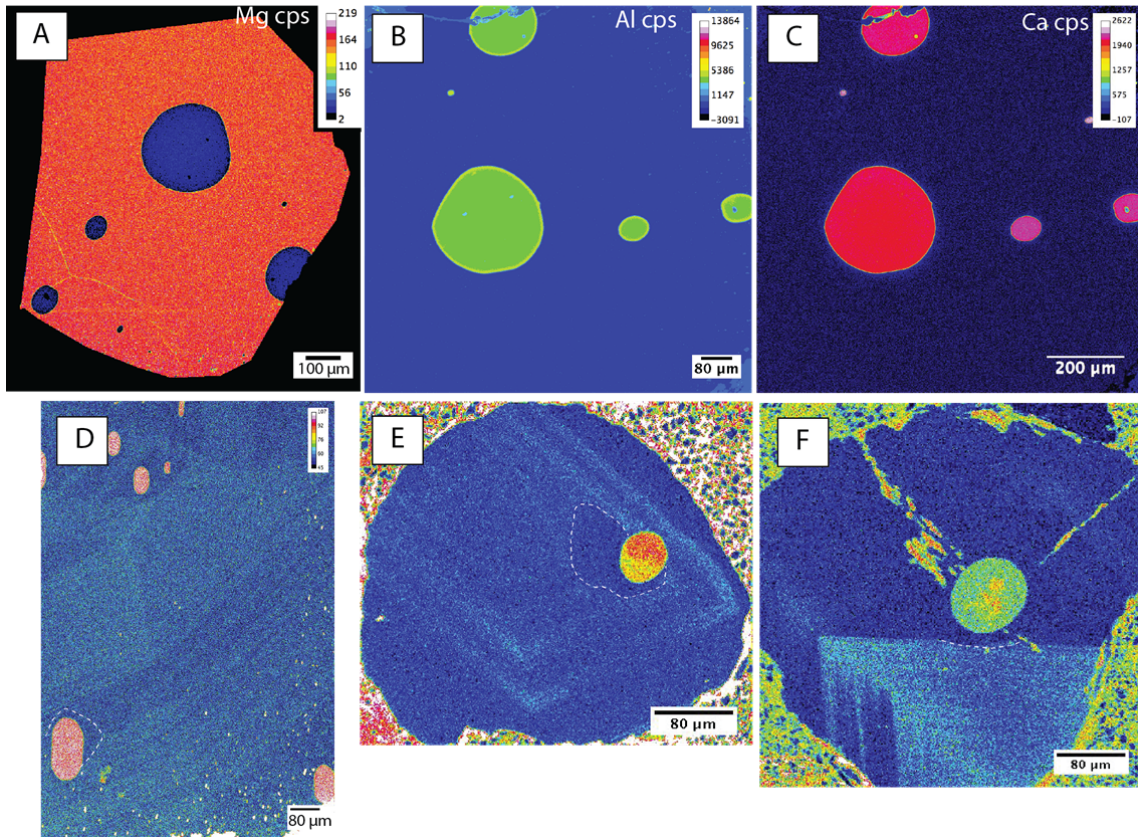
103 **Figures**

104



105

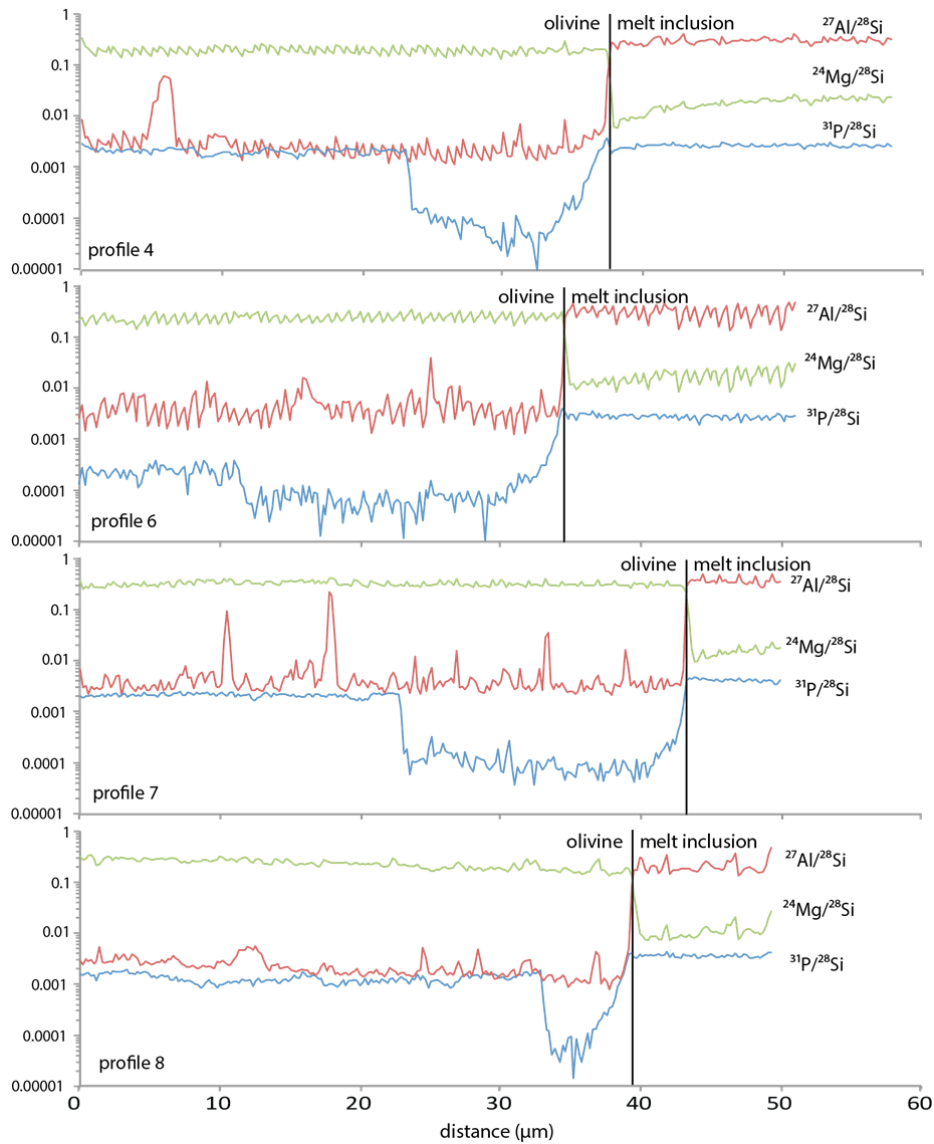
106 Figure DR1: Plot of $^{31}\text{P}/^{28}\text{Si}$ ratios obtained during NanoSIMS measurements versus (a) ^{48}Si
107 counts and (b) ^{31}P counts. The absence of correlation in (a) and the good correlation in (b)
108 indicates that $^{31}\text{P}/^{28}\text{Si}$ ratio depends on ^{31}P concentration only.



109

110 Figure DR2: X-ray maps for A- Mg concentration in ARP73-10-03_16; B- Al concentration
 111 in ARP73-10-03_16; C- Ca concentration in ARP73-10-03_16; D- P concentration in CH77-
 112 DR6-203_52; E- P concentration in CH77-DR6-203_4; F- P concentration in CH77-DR6-
 113 203_8. Note the homogeneity of the olivine in major elements (A, B and C), whereas nice P
 114 zonations are present in the same olivine (Figure 1). MI are homogeneous in P, except in Fig.
 115 DR2-E. Apparent heterogeneity of this specific MI is explained by the presence of a previous
 116 SIMS analysis spot, creating a small topography, able to slightly modify the P signal during P
 117 imaging by EMPA.

118



119

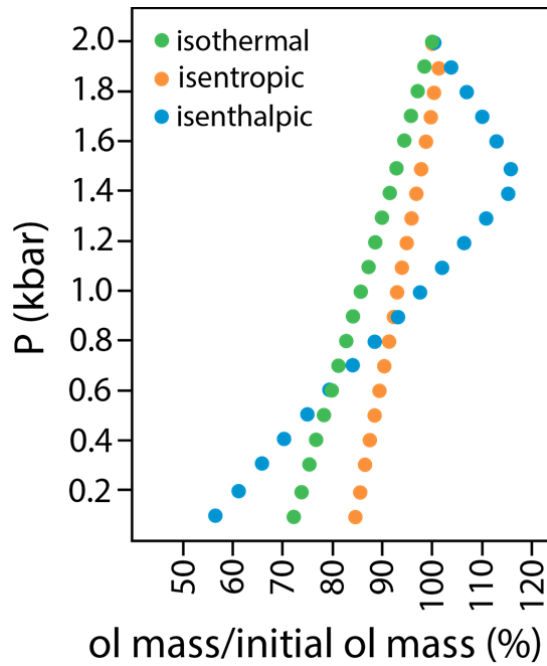
120 Figure DR3:

121 $^{31}\text{P}/^{28}\text{Si}$ profiles realized in the ARP73-10-03_16 olivine and melt inclusions for all the
 122 measured elements. The contact between MI and olivine can be determined based on the Mg
 123 and Al profiles. The location of the profiles is presented in Figure 1.

124

125

126

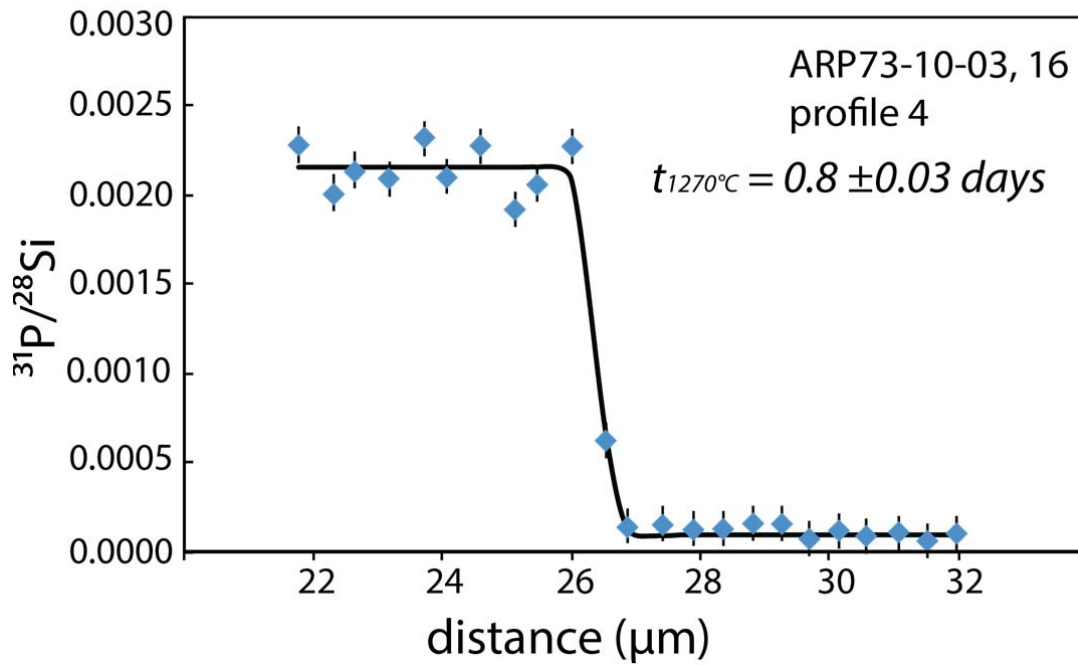


127

128 Figure DR4: Results of the MELTS decompression calculations at fixed fO_2 (QFM) between
 129 2 to 0.1 kbar for isothermal, isenthalpic and isentropic decompression. Ol is for olivine.
 130 Isentropic and isenthalpic decompression causes weak to moderate initial resorption, while
 131 isothermal decompression only causes crystallization.

132

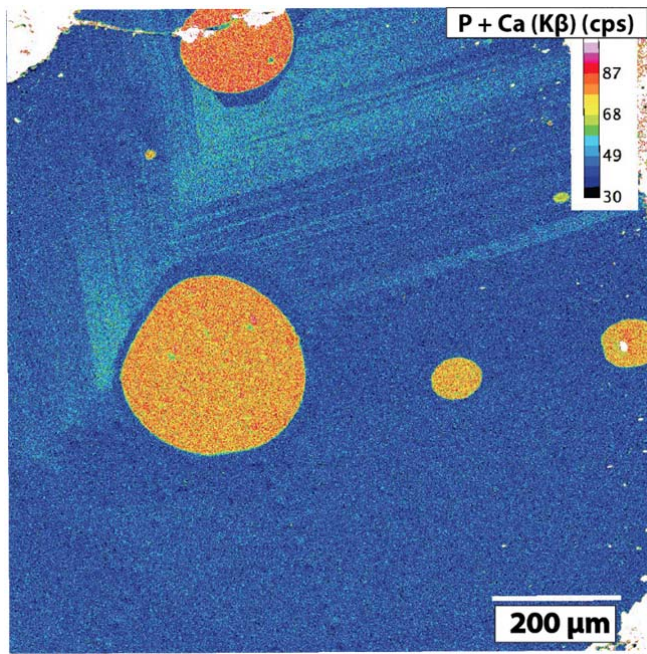
133



134

135 Figure DR5: Comparison of the measured $^{31}\text{P}/^{28}\text{Si}$ profile in olivine with the calculated curve
 136 derived from semi-infinite source diffusion modeling for profile 9, at the contact between P-
 137 rich olivine and P-depleted halo. Diffusion was 0.8 days at 1270°C , using D from Watson et
 138 al. (2015). This estimated time scale is a maximum, since the profile is near vertical, and its
 139 width is constraint by one point which could represent an analytical artefact. In fact, the
 140 profile width could be significantly overestimated.

141



142

143 Figure DR6: P distribution in ARP73-10-03_16 olivine.

144

145 **Tables**

146 Table DR1

147 NanoSIMS measurements of the profile 9 realized in the ARP73-10-13_16 olivine.

148

Table DR1

Distance (um)	31P (cps)	28Si (cps)
18.0858400	19	97678
18.3477400	26	121670
18.5226800	11	111065
18.7845900	18	126832
18.9595300	18	108121
19.2214400	24	125457
19.3963800	23	105542
19.6582900	34	142189
19.8332200	41	147602
20.0951400	37	145394
20.2700700	37	111402
20.5319900	46	127164
20.7069200	44	102883
20.9688400	72	126160
21.1437600	82	100907
21.4056900	136	117867
21.5806100	92	101973
21.8425400	159	124376
22.0174600	148	106587
22.2793900	149	122282
22.4543000	133	101183
22.7162500	182	119846
22.8911500	157	109615
23.1531000	194	127241
23.3280000	149	108946
23.5899500	145	125116
23.7648500	147	105254
24.0268000	164	124435
24.2017000	125	104253
24.4636500	143	126520
24.6385400	107	108187
24.9005000	93	127452
25.0753900	70	112467
25.3373500	42	129259
25.5122400	33	109530
25.7742000	42	122799
25.9490900	32	109173
26.2110500	42	126676
26.3859400	20	111107

Distance (um)	31P (cps)	28Si (cps)
26.6479000	20	133279
26.8227900	21	112554
27.0847500	27	135998
27.2596300	24	119142
27.5216000	33	127031
27.6964800	32	133735
27.8716300	27	115507
28.1333300	23	123117
28.3084800	16	108431
28.5701800	26	124510
28.7453200	17	109618
29.0070300	20	133930
29.1821600	14	126906
29.4438800	23	134133
29.6190000	27	145317
29.8807300	25	147300
30.0558500	25	115786
30.3175800	23	136501
30.4926900	16	126328
30.7544300	24	129967
30.9295300	18	117576
31.1912700	15	135174
31.3663800	18	116562
31.6281200	18	136904
31.8032200	23	121893
32.0649700	22	130770
32.2400700	15	118591
32.5018200	17	142127
32.6769100	15	120532
32.9386700	25	137011
33.1137600	19	121271
33.3755200	32	134642
33.5506000	22	120888
33.8123700	27	136803
33.9874500	20	119072
34.2492200	21	125619
34.4242900	12	106236
34.6860700	14	126237
34.8611400	12	110990

149 Table DR2

150 Major element compositions (determined by EPMA) and P concentration (determined by
151 SIMS) of the melt inclusions hosted in the ARP73-10-13_16 olivine. Values measured for
152 ML3B glass, used as external standard for EPMA glass analyses, are also reported. Major
153 element concentrations are given in wt% and P concentrations in ppm. For ML3B FeO
154 represents FeO_{tot} .

Table DR2

Sample	SiO2	TiO2	Al2O3	Fe2O3	FeO	MnO	MgO	CaO	Na2O	K2O	% ol added	P (ppm)	2sd%
ARP73_16a	49.52	0.59	14.42	0.91	7.83	0.12	12.07	12.96	1.51	0.07	10.9	374	0.07
ARP73_16b	49.81	0.53	14.44	0.88	7.58	0.09	11.68	13.41	1.51	0.08	12.7	495	0.06
ARP73_16c	49.71	0.55	14.53	0.87	7.63	0.14	11.80	13.28	1.43	0.06	17.0	297	0.09
ARP73_16d	48.97	0.59	14.85	0.90	7.77	0.12	11.83	13.33	1.57	0.07	17.3	311	0.08
ML3B	51.56	2.10	13.72	n.d.	11.59	0.17	6.59	10.33	2.52	0.39		n.d.	

156 Table DR3

157 Results of the MELTs calculations for the three different models tested.

Table DR3

isothermal decompression				isentropic decompression				isenthalpic decompression			
T (C)	P (kbars)	mass (mg)	forsterite	T (C)	P (kbars)	mass (mg)	forsterite	T (C)	P (kbars)	mass (mg)	forsterite
1240	2	5.194	84.27	1250	2	4.1818	84.70	1230	2	5.2288	83.59
1240	1.9	5.1211	84.30	1248.7	1.9	4.242	84.67	1229.6	1.9	5.3998	83.65
1240	1.8	5.0479	84.33	1248.3	1.8	4.2044	84.69	1229.1	1.8	5.5621	83.71
1240	1.7	4.9744	84.36	1248	1.7	4.1666	84.71	1228.6	1.7	5.7184	83.76
1240	1.6	4.9005	84.40	1247.6	1.6	4.1286	84.72	1228.1	1.6	5.8691	83.82
1240	1.5	4.8262	84.43	1247.2	1.5	4.0904	84.74	1227.6	1.5	6.0147	83.87
1240	1.4	4.7516	84.46	1246.9	1.4	4.0521	84.76	1227.6	1.4	5.9872	83.92
1240	1.3	4.6767	84.50	1246.5	1.3	4.0135	84.77	1229.2	1.3	5.7603	84.02
1240	1.2	4.6014	84.53	1246.1	1.2	3.9748	84.79	1230.7	1.2	5.5322	84.12
1240	1.1	4.5258	84.56	1245.8	1.1	3.936	84.81	1232.3	1.1	5.303	84.23
1240	1	4.4498	84.60	1245.4	1	3.8969	84.83	1233.8	1	5.0728	84.33
1240	0.9	4.3735	84.63	1245	0.9	3.8577	84.84	1235.4	0.9	4.8414	84.43
1240	0.8	4.2968	84.66	1244.6	0.8	3.8182	84.86	1236.9	0.8	4.6089	84.53
1240	0.7	4.2197	84.70	1244.3	0.7	3.7787	84.88	1238.5	0.7	4.3753	84.63
1240	0.6	4.1423	84.73	1243.9	0.6	3.7389	84.90	1240	0.6	4.1406	84.73
1240	0.5	4.0645	84.77	1243.5	0.5	3.6989	84.92	1241.6	0.5	3.9048	84.83
1240	0.4	3.9864	84.80	1243.2	0.4	3.6588	84.94	1243.1	0.4	3.6678	84.93
1240	0.3	3.9079	84.83	1242.8	0.3	3.6185	84.95	1244.6	0.3	3.4297	85.03
1240	0.2	3.829	84.87	1242.4	0.2	3.578	84.97	1246.1	0.2	3.1905	85.13
1240	0.1	3.7497	84.90	1242	0.1	3.5373	84.99	1247.6	0.1	2.9501	85.23

167 **References**

- 168 Crank, J., 1975. The mathematics of diffusion, Oxford University Press.
169 doi:10.1016/0306-4549(77)90072-X
- 170 Danyushevsky, L. V., Plechov, P., 2011. Petrolog3: Integrated software for
171 modeling crystallization processes. *Geochemistry, Geophys. Geosystems*
172 12. doi:10.1029/2011GC003516
- 173 Danyushevsky, L. V, Della, F.N., Sokolov, S., 2000. Re-equilibration of melt
174 inclusions trapped by magnesian olivine phenocrysts from subduction-
175 related magmas : petrological implications. *Contrib. to Mineral. Petrol.* 138,
176 68–83.
- 177 Danyushevsky, L. V, Sokolov, S., Falloon, T.J., 2002. Melt Inclusions in
178 Olivine Phenocrysts : Using Diffusive Re-equilibration to Determine the
179 Cooling History of a Crystal , with Implications for the Origin of Olivine-
180 phyric Volcanic Rocks. *J. Petrol.* 43, 1651–1671.
181 doi:10.1093/petrology/43.9.1651
- 182 Ghiorso, M.S., Sack, R.O., 1995. Chemical mass transfer in magmatic processes
183 IV . A revised and internally consistent thermodynamic model for the
184 interpolation and extrapolation of liquid-solid equilibria in magmatic
185 systems at elevated temperatures and pressures. *Contrib. to Mineral. Petrol.*
186 119, 197–212.
- 187 Press, W.H., Flannery, B.P., Teukolsky, S.A., Vetterling, A. t., 1992. *Numerical*
188 *Recipes in C: The Art of Scientific Computing.* New York, cambrige Univ.
189 Press 2nd ed, 994 p.
- 190 Watson, E.B., Cherniak, D.J., Holycross, M.E., 2015. Diffusion of phosphorus
191 in olivine and molten basalt. *Am. Mineral.* 100, 2053–2065.
192 doi:10.2138/am-2015-5416
- 193 Welsch, B., Hammer, J., Hellebrand, E., 2014. Phosphorus zoning reveals
194 dendritic architecture of olivine. *Geology* 42, 867–870.
195 doi:10.1130/G35691.1